

# Spin Liquid Landscapes in the Kagome Lattice: A Variational Monte Carlo Study of the Chiral Heisenberg Model and Experimental Signatures

Hee Seung Kim,<sup>1,\*</sup> Hyeok-Jun Yang,<sup>2,†</sup> Karlo Penc,<sup>3,‡</sup> and SungBin Lee<sup>1,§</sup>

<sup>1</sup>*Department of Physics, Korea Advanced Institute of Science and Technology, Daejeon, 34141, Republic of Korea*

<sup>2</sup>*Department of Physics, University of Notre Dame, South Bend, IN 46556*

<sup>3</sup>*Institute for Solid State Physics and Optics, HUN-REN Wigner*

*Research Centre for Physics, P.O. Box 49, H-1525 Budapest, Hungary*

Chiral spin liquids, which break time-reversal symmetry, are of great interest due to their topological properties and fractionalized excitations (anyons). In this work, we investigate chiral spin liquids (CSL) on the kagome lattice arising from the competition between the third-nearest-neighbor Heisenberg interaction across hexagons ( $J_d$ ) and a staggered scalar spin chirality term ( $J_\chi$ ). Using variational Monte Carlo methods, we map out the phase diagram and identify various gapped and gapless CSL phases, each characterized by a distinct flux pattern. Notably, the interplay between  $J_d$  and  $J_\chi$  induces a tricritical point, which we analyze using Landau-Ginzburg theory. Additionally, we identify potential signatures of these CSLs—including distinctive spin-spin correlations, anomalies in the static spin structure factor, longitudinal thermal conductivity, and magnetoelectric effects—which offer practical guidance for their future experimental detection.

*Introduction*—Quantum spin liquids (QSL) are receiving significant attention in both theoretical and experimental research due to their exotic properties, such as long-range entanglement in the absence of any magnetic ordering<sup>1–5</sup>. Especially in the anti-ferromagnetic Heisenberg model on the kagome lattice, the precise nature of the QSL ground state is still under debate. Notable ground-state candidates include a  $\mathbb{Z}_2$  gauge structure with a gapped spectrum<sup>6–8</sup> and a  $U(1)$  gauge structure with a gapless Dirac dispersion<sup>9–12</sup>. Among the various QSLs on the kagome lattice, the chiral spin liquid (CSL), which breaks the time-reversal symmetry  $\mathcal{T}$  (and parity symmetry depending on the lattice structure), has gained particular interest due to its topologically protected edge modes, quantized thermal Hall conductance, and anyonic statistics<sup>13–29</sup>. Recently, density matrix renormalization group and variational Monte Carlo (VMC) studies on the kagome lattice found evidence for a CSL by considering extended Heisenberg model up to third neighbor interaction on the kagome lattice<sup>19,30,31</sup>. According to Ref. 13, this CSL also includes the case with only nearest neighbor Heisenberg exchanges.

There are two well-known CSLs on the kagome lattice: the Kalmeyer-Laughlin type, which breaks reflection symmetry  $\sigma$  but preserves  $\sigma\mathcal{T}$ , and the staggered flux type, which breaks the six-fold rotation symmetry  $C_6$  but preserves  $C_6\mathcal{T}$ <sup>32,33</sup>. While these two types of CSLs are well-known, the kagome lattice allows for numerous other CSL classes, each characterized by different projective symmetry groups<sup>14</sup>. However, only a few microscopic spin Hamiltonians are known to realize these CSL classes as ground states on the kagome lattice.

In this paper, we revisit the spin-1/2  $J_1$ - $J_d$ - $J_\chi$  microscopic model on the kagome lattice<sup>26</sup>, using variational Monte Carlo (VMC) methods to investigate the realization of different classes of chiral spin liquids (CSLs). The Hamiltonian of the model is given by

$$\hat{\mathcal{H}} = J_1 \sum_{\langle i,j \rangle} \hat{\mathbf{S}}_i \cdot \hat{\mathbf{S}}_j + J_d \sum_{\langle\langle (i,j) \rangle\rangle \in \square} \hat{\mathbf{S}}_i \cdot \hat{\mathbf{S}}_j \quad (1)$$

$$+ J_\chi \left[ \sum_{ijk \in \Delta} \hat{\mathbf{S}}_i \cdot (\hat{\mathbf{S}}_j \times \hat{\mathbf{S}}_k) - \sum_{ijk \in \nabla} \hat{\mathbf{S}}_i \cdot (\hat{\mathbf{S}}_j \times \hat{\mathbf{S}}_k) \right],$$

where  $\hat{\mathbf{S}}_i$  is a spin-1/2 operator at site  $i$ , the  $J_1 = 1$  is the nearest-neighbor and  $J_d > 0$  the third-neighbor anti-ferromagnetic Heisenberg exchange across the hexagons. We also include the scalar spin chiral interaction,  $J_\chi$ , where the summations  $ijk$  run over all triangular plaquettes of the lattice, with the sites  $i$ ,  $j$ , and  $k$  ordered in the clockwise direction. The opposite sign for upward-pointing triangles ( $\Delta$ ) and downward-pointing triangles ( $\nabla$ ) results in a staggered pattern of chirality<sup>34</sup>. The  $J_\chi$  term breaks both  $\mathcal{T}$  and  $C_6$  individually, but preserves their product  $C_6\mathcal{T}$ .

*Variational Monte Carlo*—To construct possible QSL states of Hamiltonian (1), we start with a fermionic mean-field Hamiltonian,

$$\hat{\mathcal{H}}_{\text{MF}} = \sum_{\langle ij \rangle, \alpha} \left( t_{ij} \hat{f}_{i\alpha}^\dagger \hat{f}_{j\alpha} + h.c. \right). \quad (2)$$

Here  $\hat{f}_{i\alpha}$  are fermionic spinon operator that represent the spin operator as  $\hat{\mathbf{S}}_i = \frac{1}{2} \sum_{\alpha, \beta = \uparrow, \downarrow} \hat{f}_{i\alpha}^\dagger \boldsymbol{\sigma}_{\alpha\beta} \hat{f}_{i\beta}$ , where  $\boldsymbol{\sigma} = (\sigma^x, \sigma^y, \sigma^z)$  is a vector of Pauli matrices, and  $\hat{n}_i = \sum_{\alpha} \hat{f}_{i\alpha}^\dagger \hat{f}_{i\alpha}$  is the spinon number operator at site  $i$ . The ground state of the mean-field Hamiltonian is a Fermi sea of spinons, denoted as  $|\Psi_{\text{MF}}\rangle$ . We consider a half-filled system with the number of spinons equal to the number of sites,  $\langle \Psi_{\text{MF}} | \sum_{i=1}^N \hat{n}_i | \Psi_{\text{MF}} \rangle = N$ . To eliminate the spinon-number fluctuations, we use the variational

\* shamoo0829@kaist.ac.kr

† hyang23@nd.edu

‡ penc.karlo@wigner.hun-ren.hu

§ sungbin@kaist.ac.kr

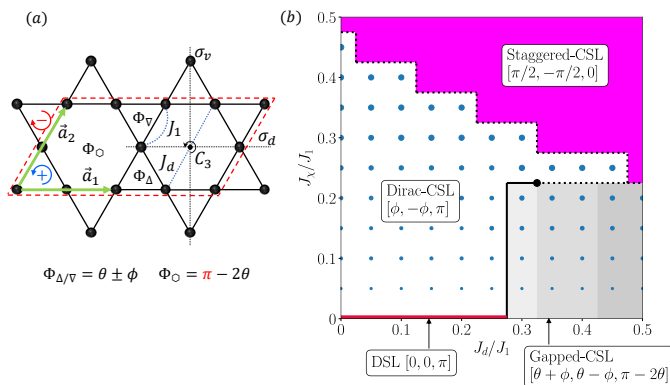


FIG. 1. (a) The flux pattern of Eq. (2) on the kagome lattice. The  $U(1)$  gauge fluxes are  $\Phi_{\Delta/\nabla} = \theta \pm \phi$  through the up/down triangles and  $\Phi_{\circ} = -2\theta$  through the hexagons. The red dotted line indicates the enlarged unit cell of the type-1 flux pattern. The fermionic spinon hopping amplitude is  $|t_{ij}| = 1$  for all nearest neighbor pairs. (b) Variational Monte Carlo phase diagram of the  $J_1 - J_d - J_{\chi}$  model for a  $N = 3 \times 12^2$  site cluster. We identify four distinct phases: the Dirac spin liquid (DSL), the Dirac chiral spin liquid (Dirac CSL), the gapped chiral spin liquid (gapped CSL), and the staggered chiral spin liquid (staggered CSL). The size of the blue circles represents the magnitude of the staggered flux  $\phi$ , while the intensity of the gray shading is proportional to the value of  $\theta$ , where  $\Phi_{\circ} = \pi - 2\theta$ . In the magenta region  $\phi = \pi/2$ ,  $\theta = 0$ , and  $\Phi_{\circ} = 0$ . The flux patterns and point group symmetries of each phase are detailed in Table I. Solid lines represent second-order phase transition boundaries, while dotted lines indicate first-order transitions.

wave function  $|\Psi_G\rangle \equiv P_G |\Psi_{MF}\rangle$ , where the Gutzwiller projection  $P_G = \prod_i \hat{n}_i(2 - \hat{n}_i)$  ensures that the half-filling condition is satisfied at each site. We focus on different compact  $U(1)$  gauge flux patterns to characterize the QSL phases. Specifically, we consider uniform nearest neighbor hopping amplitudes with  $|t_{ij}| = 1$  and minimize the variational energy,  $\langle \Psi_G | \hat{\mathcal{H}} | \Psi_G \rangle$  with respect to the  $U(1)$  gauge fluxes through the lattice.

Each unit cell comprises three plaquettes: the up- and down-pointing triangles and the hexagon. We introduce two parameters to characterize the chiral QSL states: a uniform flux  $\theta$  and a staggered flux  $\phi$  through the triangles. Then, the total flux through the up triangles is  $\Phi_{\Delta} = \theta + \phi$  and the down triangles is  $\Phi_{\nabla} = \theta - \phi$ . The flux of the hexagonal plaquettes,  $\Phi_{\circ}$ , can take one of two forms depending on the type of flux pattern: for type-1,  $\Phi_{\circ} = \pi - 2\theta$ ; for type-2,  $\Phi_{\circ} = -2\theta$  (see Fig. 1(a)). For type-1, the total flux threading the elementary unit cell is  $\pi$ , requiring a doubled unit cell size in our calculations. By specifying the gauge fluxes on these three plaquettes, we can uniquely distinguish different QSL states, which we denote as  $SL[\Phi_{\Delta}, \Phi_{\nabla}, \Phi_{\circ}]$ .

We performed VMC calculations on a finite system consisting of  $N = 3 \times 12 \times 12$  lattice sites. The finite-size mean-field spectrum depends on the choice of the gauge fluxes  $(\theta, \phi)$ , and in certain cases, degenerate states ap-

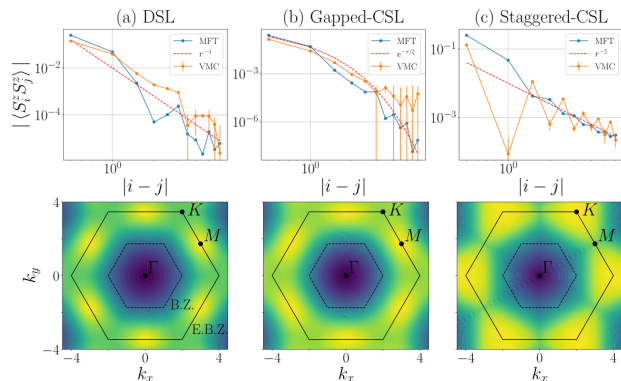


FIG. 2. (Top) Spin-spin correlation of (a) Dirac spin liquid (DSL), (b) gapped chiral spin liquid (gapped CSL), and (c) staggered chiral spin liquid (staggered CSL). We plot variational Monte Carlo (VMC) and mean-field results for each case. (Bottom) Corresponding static spin structure factor. The dotted and solid lines in the bottom figures represent the 1st and the extended Brillouin zone, respectively. The structure factor is normalized over the extended Brillouin zone,  $\sum_{\mathbf{q} \in \text{EBZ}} S(\mathbf{q}) = 1$ .

pear at the Fermi level. This degeneracy leads to ambiguity in selecting the mean-field ground state  $|\Psi_{MF}\rangle$ , making the half-filled ground state not uniquely defined. To address this problem, we applied twisted boundary conditions to shift the momentum grid in the  $\mathbf{k}$ -space, thereby lifting the degeneracy. However, these twisted boundary conditions spoil the symmetry of the momentum grid, breaking the  $C_6$  rotational symmetry of the original Hamiltonian. Consequently, the Gutzwiller-projected wave function constructed from this asymmetric momentum grid does not preserve the  $C_6$  symmetry and introduces biases in calculated physical quantities such as spin-spin correlations. To restore the symmetry, we constructed a fully symmetric Gutzwiller-projected wave function by superposing wave functions from different boundary conditions connected by point group symmetries, as detailed in Appendix A.

*Phase diagram*— In the absence of chiral term ( $J_{\chi} = 0$ ), the time-reversal invariant  $SL[0, 0, \pi]$  state minimizes the energy for small  $J_d < J_d^c \approx 0.25 \sim 0.3$ . The spinon band structure features two Dirac cones within the reduced Brillouin zone and goes under the name “Dirac spin liquid” (DSL)<sup>9,11,12,35</sup>. The Dirac cones in the mean-field spectrum are protected by  $\sigma_d$ <sup>33</sup>. Despite the unit cell doubling caused by the  $\pi$  flux, the projective symmetry group restores the full translational and  $D_{6h}$  point group symmetries of the kagome lattice.

As  $J_d$  increases above the critical value  $J_d^c$ , the system stabilizes a state that spontaneously breaks the time-reversal symmetry, the CSL with the flux pattern labeled by  $SL[\theta, \theta, \pi - 2\theta]$ . Since this flux pattern also breaks the  $\sigma_d$  symmetry that protects the Dirac cones, a gap opens inside the bulk, and the bands get finite Chern numbers. This state, known as the gapped chiral spin

TABLE I. The flux patterns  $\text{SL}[\Phi_\Delta, \Phi_\nabla, \Phi_\circ]$ , the decay of the  $|S_i^z S_j^z|$  spin-spin correlations and of the  $\kappa_{xx}$  thermal conductivity, the magnetic point groups and the magnetoelectric invariant for the different flux states.

	DSL	Dirac CSL	staggered CSL	gapped CSL	gapped CSL
$\text{SL}[\Phi_\Delta, \Phi_\nabla, \Phi_\circ]$	$\text{SL}[0,0,\pi]$	$\text{SL}[\phi, -\phi, \pi]$	$\text{SL}[\pi/2, -\pi/2, 0]$	$\text{SL}[\theta, \theta, \pi - 2\theta]$	$\text{SL}[\theta + \phi, \pi - 2\theta]$
$ S_i^z S_j^z $	$ i - j ^{-4}$	$ i - j ^{-4}$	$ i - j ^{-2}$	Exp. decay	Exp. decay
$\kappa_{xx}$	Power law		Power law	Exp. decay	Exp. decay
Sym. group	$\{1, \mathcal{T}\} \otimes \text{D}_{6h}$	$\{1, \mathcal{T}\sigma_v\} \otimes \text{D}_{3h}$		$\{1, \mathcal{T}\sigma_v\} \otimes \text{C}_{6h}$	$\{1, \mathcal{T}\sigma_v\} \otimes \text{C}_{3h}$
$P_y^3 - 3P_x^2 P_y, 2P_x M_x M_y + P_y(M_x^2 - M_y^2)$	-		-	-	inv.
$M_z, (P_x M_x + P_y M_y) P_z$	-		-	inv.	inv.
$P_z [2P_x P_y M_x + (P_x^2 - P_y^2) M_y]$	-		inv.	-	inv.
$M_z [2M_x M_y P_x + (M_x^2 - M_y^2) P_y]$	-		inv.	-	inv.
$(M_y^3 - 3M_x^2 M_y) P_z, (P_y^3 - 3P_x^2 P_y) M_z$	-		inv.	-	inv.
$P_x^2 + P_y^2, P_z^2, M_x^2 + M_y^2, M_z^2$	inv.		inv.	inv.	inv.

liquid (gapped CSL), is an analog of fractional quantum Hall state with the filling factor  $\nu = 1/2$ <sup>31,36</sup>.

A finite  $J_\chi$  in Eq. (1) explicitly breaks  $\mathcal{T}$  symmetry in a staggered manner, and the ground state tends to trap opposite gauge fluxes on the up and down triangles, leading to nonzero staggered flux  $\phi \neq 0$ . Consequently, a finite  $J_\chi$  introduces a phase transition from DSL to a new type of CSL, characterized by  $\text{SL}[\phi, -\phi, \pi]$ . Although this flux pattern breaks  $\mathcal{T}$  symmetry, it still preserves horizontal reflection symmetry. As a result, the Dirac cones remain gapless. This state is called the Dirac chiral spin liquid (Dirac CSL). As  $J_\chi$  increases, the staggered chiral flux  $\phi$  in the Dirac spin liquid (DSL) phase grows continuously. This continuous rise persists until a first-order transition occurs, leading to the staggered chiral spin liquid phase, which we will discuss later. According to Table IX of Ref. 33, Dirac CSL corresponds to No. 12 among staggered flux  $U(1)$  CSL phases, marking its first realization of non-Fermi liquids with Dirac Fermi surfaces of fractionalized excitations.

Similarly, starting from a gapped CSL,  $\text{SL}[\theta, \theta, \pi - 2\theta]$ , a staggered flux  $\phi$  appears as  $J_\chi$  increases. This results in the flux pattern  $\text{SL}[\theta + \phi, \theta - \phi, \pi - 2\theta]$ . Although a finite  $\phi$  reduces the rotational symmetry from  $C_6$  to  $C_3$ , it preserves the spinon gap structure and the associated fractional quantum Hall state. Therefore, we consider this the same gapped CSL phase as the  $\phi = 0$  case for  $J_\chi = 0$ . However, the electromagnetic response will differ due to the reduced symmetry, as we will discuss in the experimental probes section.

For small values of  $J_\chi$ , the phase transition between the Dirac spin liquid (DSL) and the gapped chiral spin liquid (CSL) is continuous. However, as  $J_\chi$  increases further, this transition becomes discontinuous (first-order). The tricritical point where the nature of the transition changes from continuous to discontinuous is indicated by the black circle in Fig. 1 (b). We provide a detailed

Landau-Ginzburg analysis of these phase transitions in terms of the parameters  $\theta$  and  $\phi$  in Appendix D.

For sufficiently large  $J_\chi$ , the fluxes on the triangles reach their maximum values,  $\Phi_\Delta = -\Phi_\nabla = \pi/2$ . Simultaneously, the flux on the hexagon stabilizes at  $\Phi_\circ = 0$  (type-2) rather than  $\Phi_\circ = \pi$  (type-1), i.e.,  $\text{SL}[\pi/2, -\pi/2, 0]$ . This state is called a staggered chiral spin liquid (staggered CSL). The mean-field spectrum is gapless and exhibits a line degeneracy at the Fermi level along the vertical reflection symmetry line, protected by the anti-commutation relation  $\{\hat{\mathcal{H}}_{\text{MF}}, \sigma_v\} = 0$ <sup>25</sup>, as discussed in Appendix C. In Ref. 26, the authors suggested a purely imaginary nearest-neighbor hopping mean-field amplitude in the fermionic spinon basis for the large  $J_\chi$  limit as a prominent example of non-Fermi liquids. This mean-field approach generates  $\pm\pi/2$  fluxes through the up and down triangles. We confirm that this staggered flux pattern with  $\Phi_\Delta = -\Phi_\nabla = \pi/2$  yields the minimum variational energy, even if we treat the flux as a variational parameter for large  $J_\chi$ . The staggered CSL corresponds to No. 11 in the staggered flux  $U(1)$  CSL phases in Table IX of Ref. 33.

*Experimental probes*— We begin by presenting the absolute value of the spin-spin correlation function,  $|\langle S_i^z S_j^z \rangle|$ , for (a) DSL, (b) gapped CSL, and (c) staggered CSL calculated by VMC simulations in Fig. 2. Because they are gapless, both the DSL and the staggered CSL exhibit algebraic decay of spin correlations,  $|\langle S_i^z S_j^z \rangle| \propto |i - j|^{-\alpha}$ , but with different exponent:  $\alpha \approx 4$  in the DSL<sup>35</sup> and  $\alpha \approx 2$  in the staggered CSL. We also compare the decay of the spin correlations in real space with predictions from mean-field theory in Fig. 2(a) and (c). In contrast, the spin correlations decay exponentially in the gapped CSL, as shown in Fig. 2(b).

The bottom row of Fig. 2 displays the static spin struc-

ture factor  $S^{zz}(\mathbf{q})$ ,

$$S^{zz}(\mathbf{q}) = \sum_{i,j} e^{i\mathbf{q}\cdot(\mathbf{r}_i-\mathbf{r}_j)} \langle S_i^z S_j^z \rangle. \quad (3)$$

The structure factor of the DSL peaks at the  $M$  points of the extended Brillouin zone<sup>35</sup>. The position of the peaks agrees with the classical calculation result, the so-called  $q = 0$  phase<sup>37</sup>. The peak positions in the gapped CSL phase remain at the  $M$  points but are blurred compared to the DSL due to the spinon gap opening [Fig. 2 (b)]. Finally, the structure factor of the staggered CSL is maximal at the  $K$  point [Fig. 2 (c)], showing a completely different behavior than the other phases. In the presence of the staggered chirality term, the classical spins order in a so-called cuboc-1 state, with a structure factor showing peaks also near the  $K$  points<sup>26</sup>.

Next, we turn our attention to thermal conductivity as a means to probe the excitations and their dispersions in the system since heat transport is facilitated by these excitations. At the mean-field level, ignoring gauge fluctuations, spinons are the primary degrees of freedom. Therefore, we examine the low-temperature behavior of the longitudinal thermal conductivity tensor  $\kappa_{xx}$ <sup>38–40</sup>. In the DSL, Dirac CSL, and staggered CSL phases,  $\kappa_{xx}$  follows a power-law dependence on temperature due to gapless spinon dispersions. In contrast, the longitudinal thermal conductivity of the gapped CSL decays exponentially with decreasing temperature, with the decay rate determined by the size of the spinon band gap.

Finally, we consider the response to the electric field. For finite values of  $\theta$  and  $\phi$ , the ground state breaks the grey magnetic point group  $\{1, \mathcal{T}\} \otimes D_{6h}$  of the kagome lattice, as illustrated in Fig. 3. Consequently, the reduced symmetry leads to a coupling between magnetization  $\mathbf{M} = (M^x, M^y, M^z)$  and electric polarization  $\mathbf{P} = (P^x, P^y, P^z)$ , where  $\mathbf{M} = \sum \mathbf{S}_i$ . Table I lists the symmetry-allowed invariants. For example, for finite values of  $\phi$ , the  $(M_y^3 - 3M_x^2 M_y) P_z$  becomes an invariant. Consequently, rotating the magnetic field by an angle  $\eta$  within the plane of the kagome lattice can induce an out-of-plane electric polarization  $P_z$  that varies with  $\cos 3\eta$ . This behavior is analogous to the magnetoelectric response observed in  $\text{Ba}_2\text{CoGe}_2\text{O}_7$ <sup>41</sup>. The various forms of these invariants enable the identification of the broken symmetries in the system and, consequently, of the flux structure of the spin liquid. See Appendix B for details.

We also explored the microscopic origin of the magnetoelectric coupling. A finite scalar chirality emerges in a third-order hopping process in a Mott insulator when a finite flux threads through a triangle and couples via the Peierls phase to the charges<sup>42</sup>. Similarly, asymmetri-

cal  $\langle \mathbf{S}_i \cdot \mathbf{S}_j \rangle$  expectation values on the bonds of triangles lead to charge imbalance and electric polarization within the kagome plane<sup>43</sup>. We performed exact diagonalization calculations on a small, 12-site cluster to assess whether these mechanisms can reproduce the phenomenological responses. Rotating the in-plane electric field, we only found a varying total scalar chirality, with  $\mathbf{M} = 0$ . To account for finite  $P_z$  and  $\mathbf{M}$ , one must consider the spin-orbit coupling that leads to the spin-current mechanism<sup>44,45</sup>, the Dzyaloshinskii-Moriya interaction and the Kitaev-like anisotropies<sup>46,47</sup>.

*Conclusion*—Based on the VMC, we identified four distinct  $U(1)$  QSLs: Dirac spin liquid, Dirac CSL, gapped CSL, and staggered CSL. The staggered CSL has been previously studied in the large  $J_\chi$  limit, proposing a  $U(1)$  gauge flux of  $\pm\pi/2$  through up and down triangles<sup>25,26</sup>. We confirm that this flux pattern minimizes the energy by treating the  $U(1)$  gauge flux as a variational parameter. In the intermediate  $J_\chi$  regime, a new Dirac CSL phase emerges, characterized by time-reversal symmetry-breaking Dirac spinons. Our gapped CSL also exhibits distinct symmetry and flux patterns compared to earlier works<sup>19,30,31</sup>, due to the competing  $J_d$  and  $J_\chi$  terms. Additionally, the interaction between  $J_d$  and  $J_\chi$  generates a tricritical point between Dirac CSL and gapped CSL around  $(J_d/J_1, J_\chi/J_1) \sim (0.3, 0.2)$ . The emergence of the tricritical point is briefly discussed using the symmetry-allowed Landau-Ginzburg theory. As experimental probes, we propose using spin-spin correlation, spin structure factor, longitudinal thermal conductance exponent, and electromagnetic response to differentiate between these QSLs. Our work suggests new types of  $U(1)$  spin liquids grounded in microscopic spin exchange models, offering distinct possibilities for experimental differentiation. Finally, while our study focused on a specific subset of  $U(1)$  chiral spin liquids connected to the Dirac spin liquid flux pattern, numerous  $Z_2$  staggered and Kalmeyer-Laughlin-type chiral spin liquids also exist<sup>33</sup>. Extending our mean-field and VMC calculations to these  $Z_2$  states could test the robustness of our results and potentially uncover new quantum phases with exotic properties.

## ACKNOWLEDGMENTS

We thank Sándor Bordács and Yasir Iqbal for the valuable discussions. We acknowledge the financial support provided by the Korean National Research Foundation Grant (2021R1A2C109306013), the Hungarian NKFIH Grant No. K142652, and, in part, the National Science Foundation under Grant No. NSF PHY-1748958 to the Kavli Institute for Theoretical Physics (KITP).

<sup>1</sup> L. Balents, *Nature* **464**, 199 (2010).

<sup>2</sup> L. Savary and L. Balents, *Reports on Progress in Physics*



- 80, 016502 (2016).
- <sup>3</sup> J. Knolle and R. Moessner, *Annual Review of Condensed Matter Physics* **10**, 451 (2019), <https://doi.org/10.1146/annurev-conmatphys-031218-013401>.
  - <sup>4</sup> P. A. Lee, *Science* **321**, 1306 (2008), <https://www.science.org/doi/pdf/10.1126/science.1163196>.
  - <sup>5</sup> Y. Zhou, K. Kanoda, and T.-K. Ng, *Rev. Mod. Phys.* **89**, 025003 (2017).
  - <sup>6</sup> Y.-M. Lu, Y. Ran, and P. A. Lee, *Phys. Rev. B* **83**, 224413 (2011).
  - <sup>7</sup> S. Yan, D. A. Huse, and S. R. White, *Science* **332**, 1173 (2011), <https://www.science.org/doi/pdf/10.1126/science.1201080>.
  - <sup>8</sup> S. Depenbrock, I. P. McCulloch, and U. Schollwöck, *Phys. Rev. Lett.* **109**, 067201 (2012).
  - <sup>9</sup> Y. Ran, M. Hermele, P. A. Lee, and X.-G. Wen, *Phys. Rev. Lett.* **98**, 117205 (2007).
  - <sup>10</sup> Y. Iqbal, F. Becca, and D. Poilblanc, *Phys. Rev. B* **84**, 020407 (2011).
  - <sup>11</sup> Y. Iqbal, F. Becca, S. Sorella, and D. Poilblanc, *Phys. Rev. B* **87**, 060405 (2013).
  - <sup>12</sup> Y. Iqbal, D. Poilblanc, and F. Becca, *Phys. Rev. B* **89**, 020407 (2014).
  - <sup>13</sup> R.-Y. Sun, H.-K. Jin, H.-H. Tu, and Y. Zhou, *npj Quantum Materials* **9**, 16 (2024).
  - <sup>14</sup> S. Bieri, L. Messio, B. Bernu, and C. Lhuillier, *Phys. Rev. B* **92**, 060407 (2015).
  - <sup>15</sup> D. F. Schroeter, E. Kapit, R. Thomale, and M. Greiter, *Phys. Rev. Lett.* **99**, 097202 (2007).
  - <sup>16</sup> H. Yao and S. A. Kivelson, *Phys. Rev. Lett.* **99**, 247203 (2007).
  - <sup>17</sup> R. Thomale, E. Kapit, D. F. Schroeter, and M. Greiter, *Phys. Rev. B* **80**, 104406 (2009).
  - <sup>18</sup> L. Cincio and G. Vidal, *Phys. Rev. Lett.* **110**, 067208 (2013).
  - <sup>19</sup> Y.-C. He, D. N. Sheng, and Y. Chen, *Phys. Rev. Lett.* **112**, 137202 (2014).
  - <sup>20</sup> Y.-C. He, S. Bhattacharjee, F. Pollmann, and R. Moessner, *Phys. Rev. Lett.* **115**, 267209 (2015).
  - <sup>21</sup> A. Wietek and A. M. Läuchli, *Phys. Rev. B* **95**, 035141 (2017).
  - <sup>22</sup> A. Szasz, J. Motruk, M. P. Zaletel, and J. E. Moore, *Phys. Rev. X* **10**, 021042 (2020).
  - <sup>23</sup> C. Hickey, L. Cincio, Z. Papić, and A. Paramekanti, *Phys. Rev. Lett.* **116**, 137202 (2016).
  - <sup>24</sup> B. Bauer, L. Cincio, B. P. Keller, M. Dolfi, G. Vidal, S. Trebst, and A. W. W. Ludwig, *Nature Communications* **5**, 5137 (2014).
  - <sup>25</sup> B. Bauer, B. P. Keller, S. Trebst, and A. W. W. Ludwig, *Phys. Rev. B* **99**, 035155 (2019).
  - <sup>26</sup> F. Oliviero, J. A. Sobral, E. C. Andrade, and R. G. Pereira, *SciPost Phys.* **13**, 050 (2022).
  - <sup>27</sup> B. Bauer, B. P. Keller, M. Dolfi, S. Trebst, and A. W. W. Ludwig, “Gapped and gapless spin liquid phases on the kagome lattice from chiral three-spin interactions,” (2014), [arXiv:1303.6963 \[cond-mat.str-el\]](https://arxiv.org/abs/1303.6963).
  - <sup>28</sup> R. G. Pereira and S. Bieri, *SciPost Phys.* **4**, 004 (2018).
  - <sup>29</sup> A. Wietek, A. Sterdyniak, and A. M. Läuchli, *Phys. Rev. B* **92**, 125122 (2015).
  - <sup>30</sup> S.-S. Gong, W. Zhu, L. Balents, and D. N. Sheng, *Phys. Rev. B* **91**, 075112 (2015).
  - <sup>31</sup> S.-S. Gong, W. Zhu, and D. N. Sheng, *Scientific Reports* **4**, 6317 (2014).
  - <sup>32</sup> V. Kalmeyer and R. B. Laughlin, *Phys. Rev. Lett.* **59**, 2095 (1987).
  - <sup>33</sup> S. Bieri, C. Lhuillier, and L. Messio, *Phys. Rev. B* **93**, 094437 (2016).
  - <sup>34</sup> At the microscopic level, the staggered spin chiral interaction arises from anisotropic exchanges induced by spin-orbit coupling and from the influence of external magnetic fields under conditions of reduced symmetry. The forthcoming paper will elaborate on these specific mechanisms and details.
  - <sup>35</sup> M. Hermele, Y. Ran, P. A. Lee, and X.-G. Wen, *Phys. Rev. B* **77**, 224413 (2008).
  - <sup>36</sup> W.-J. Hu, W. Zhu, Y. Zhang, S. Gong, F. Becca, and D. N. Sheng, *Phys. Rev. B* **91**, 041124 (2015).
  - <sup>37</sup> F. Kolley, S. Depenbrock, I. P. McCulloch, U. Schollwöck, and V. Alba, *Phys. Rev. B* **91**, 104418 (2015).
  - <sup>38</sup> H. Mousavi, J. Khodadadi, J. Moradi Kurdestany, and Z. Yarmohammadi, *Physics Letters A* **380**, 3823 (2016).
  - <sup>39</sup> I. Paul and G. Kotliar, *Phys. Rev. B* **67**, 115131 (2003).
  - <sup>40</sup> A. V. Joura, D. O. Demchenko, and J. K. Freericks, *Phys. Rev. B* **69**, 165105 (2004).
  - <sup>41</sup> H. Murakawa, Y. Onose, S. Miyahara, N. Furukawa, and Y. Tokura, *Phys. Rev. Lett.* **105**, 137202 (2010).
  - <sup>42</sup> O. I. Motrunich, *Phys. Rev. B* **73**, 155115 (2006).
  - <sup>43</sup> L. N. Bulaevskii, C. D. Batista, M. V. Mostovoy, and D. I. Khomskii, *Phys. Rev. B* **78**, 024402 (2008).
  - <sup>44</sup> H. Katsura, N. Nagaosa, and A. V. Balatsky, *Phys. Rev. Lett.* **95**, 057205 (2005).
  - <sup>45</sup> I. A. Sergienko and E. Dagotto, *Phys. Rev. B* **73**, 094434 (2006).
  - <sup>46</sup> I. Kimchi and A. Vishwanath, *Phys. Rev. B* **89**, 014414 (2014).
  - <sup>47</sup> K. Morita, M. Kishimoto, and T. Tohyama, *Phys. Rev. B* **98**, 134437 (2018).

### Appendix A: Construction of a fully symmetrized projected wave function

In the main text, we discussed that twisted boundary conditions do not preserve the symmetry of the original Hamiltonian, leading to symmetry-breaking results in VMC calculations. We describe below how to construct a fully symmetric Gutzwiller-projected wave function to address this issue.

Let  $g$  and  $\tilde{g}$  denote two different gauge structures of the same flux pattern related by a point group symmetry operation. Let  $H_{\text{MF}}^g$  and  $H_{\text{MF}}^{\tilde{g}}$  be the corresponding  $N \times N$  mean-field Hamiltonian matrices defined on the lattice ( $N$  is the number of sites). There exists a  $U(1)$  gauge transformation  $G$  such that  $GH_{\text{MF}}^{\tilde{g}}G^\dagger = H_{\text{MF}}^g$ . Let  $V^g$  be the eigenvector matrix of  $H_{\text{MF}}^g$ , satisfying  $H_{\text{MF}}^g V^g = E V^g$ , and similarly for  $\tilde{g}$ , where  $E = \text{diag}(E_1, \dots, E_N)$  is the diagonal matrix of eigenvalues (energies). Applying the gauge transformation, we have  $GV^{\tilde{g}}E(GV^{\tilde{g}})^\dagger = V^g E V^{g\dagger}$ . We define the unitary matrix  $D \equiv V^{g\dagger} G V^{\tilde{g}}$  which satisfies  $DED^\dagger = E$ . This implies that  $D$  commutes with  $E$  and can be block-diagonalized in the energy basis. We construct the half-filled Gutzwiller-projected wave functions  $|\Psi^g\rangle$  and  $|\Psi^{\tilde{g}}\rangle$  from  $V^g$  and  $V^{\tilde{g}}$ , respectively. The relation  $GV^{\tilde{g}} = V^g D$

implies that the  $(\det G)^{-1}(\det D_{<})^2 |\Psi^g\rangle = |\Psi^{\bar{g}}\rangle$ . Assuming  $E_F$  is non-degenerate, we can divide  $D$  into block-diagonalize unitary matrices  $D_{<}$  and  $D_{>}$ , corresponding to energies below and above  $E_F$ , respectively.

We are now ready to construct the fully symmetric projected wave function. We consider periodic and anti-periodic boundary conditions with  $C_{6h}$  point group symmetry for simplicity. We assume they the number of unit cells along the primitive lattice vectors is a multiple of 4 (we found no trivial irreducible representation for other cases). Denoting periodic and anti-periodic boundary conditions by P and A, we have four different boundary conditions: [PP], [AP], [PA], and [AA], where the first and second letters represent the boundary conditions along the  $\mathbf{a}_1$  and  $\mathbf{a}_2$  directions, respectively. Let  $|\Psi_{[AP]}^g\rangle$  be the projected wave function with gauge structure  $g$  and AP boundary condition. The generators of the  $C_{6h}$  point group are the  $C_6$  and  $\sigma_h$ . The  $C_6$  connects the [AP] boundary condition with the [PA] and [AA] boundary conditions but with different gauge structures. Therefore, using the relation  $(\det G)^{-1}(\det D_{<})^2 |\Psi^g\rangle = |\Psi^{\bar{g}}\rangle$ , the action of the  $C_6$  operator can be represented as

$$C_6 \begin{pmatrix} |\Psi_{PA}^g\rangle \\ |\Psi_{AP}^g\rangle \\ |\Psi_{AA}^g\rangle \end{pmatrix} = \begin{pmatrix} 0 & e^{i\phi_1} & 0 \\ 0 & 0 & e^{i\phi_2} \\ e^{i\phi_3} & 0 & 0 \end{pmatrix} \begin{pmatrix} |\Psi_{PA}^g\rangle \\ |\Psi_{AP}^g\rangle \\ |\Psi_{AA}^g\rangle \end{pmatrix}, \quad (\text{A1})$$

where the phases satisfy  $\phi_1 + \phi_2 + \phi_3 = 0 \pmod{2\pi}$  regardless of the initial gauge choice. The  $|\Psi_{A_1}^g\rangle = |\Psi_{PA}^g\rangle + e^{i\phi_1} |\Psi_{AP}^g\rangle + e^{i\phi_1+i\phi_2} |\Psi_{AA}^g\rangle$  is invariant under the action of  $C_{6h}$  up to a global phase, ensuring that it belongs to the trivial representation. We use this fully symmetric projected wave function in our VMC calculation.

## Appendix B: Magnetoelectric coupling

In the following, we derive the symmetry-allowed interaction between magnetic and electric polarizations in different phases, known as magnetoelectric coupling. To this end, let us extend the two-dimensional point group of the kagome lattice to the three-dimensional group  $D_{6h}$  having 24 elements. A convenient set of generators includes the  $C_6$  rotation, the  $\sigma_h \equiv \sigma_{xy}$  reflection in the basal plane, and the reflection  $\sigma_d \equiv \sigma_{xz}$  about the  $y$  axis. To properly account for magnetization, we also include the antiunitary time-reversal symmetry. Since the Dirac spin liquid does not break any spatial symmetry, its magnetic point group is the grey  $\{1, \mathcal{T}\} \otimes D_{6h}$ , see Fig. 3. The Dirac CSL, the staggered CSL, and the Hamiltonian (1) with a finite  $J_\chi$  value are all invariant under the black and white point group  $\{1, \mathcal{T}\sigma_v\} \otimes D_{3h} \equiv D_{6h}(D_{3h})$ . The symmetry group of the gapped CSL with  $\phi = 0$  is  $\{1, \mathcal{T}\sigma_v\} \otimes C_{6h} \equiv D_{6h}(C_{6h})$  and  $\{1, \mathcal{T}\sigma_v\} \otimes C_{3h} \equiv D_{3h}(C_{3h})$  for finite values of  $\phi$ . All the chiral flux patterns we looked at (analyzed, examine, inspect, survey, study,

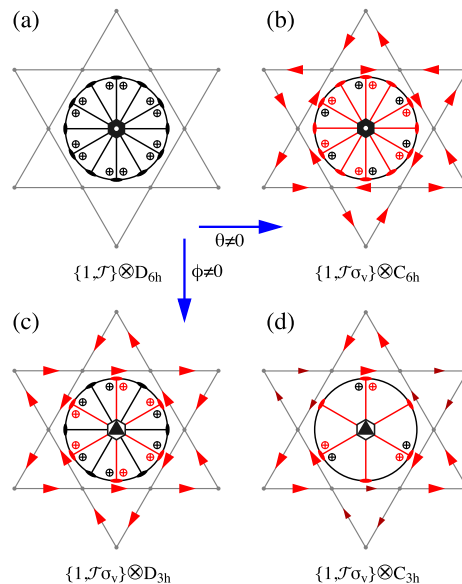


FIG. 3. Diagrams illustrating the reduction of the grey point group symmetry  $\{1, \mathcal{T}\} \otimes D_{6h}$  (a) in spin liquids with different flux patterns indicated by red arrows on the edges of the kagome lattice.  $\theta$  is finite in (b) and (d), while a staggered flux ( $\phi \neq 0$ ) is present in (c) and (d). Inside the hexagons, the stereograms represent the magnetic point group corresponding to the specific flux configuration; black symbols denote elements of the unitary subgroup, while red symbols represent elements of the antiunitary subgroup (point-group symmetry combined with  $\mathcal{T}$ ).

scrutinize, investigate, explore, probe) are invariant under the reflection  $\sigma_v$  followed by time reversal,  $\mathcal{T}\sigma_v$ , and under the unitary point group  $C_{3h}$ .

By considering the transformations of the components of the uniform magnetization  $\mathbf{M}$  and electric polarization  $\mathbf{P}$ , we can construct invariant multinomials under the symmetry group of each phase. For example, time reversal  $\mathcal{T}$  reverses magnetization,  $\mathbf{M} \rightarrow -\mathbf{M}$ , but leaves polarization unchanged,  $\mathbf{P} \rightarrow \mathbf{P}$ . The combined operation  $\mathcal{T}\sigma_v$  transforms  $(M_x, M_y, M_z) \rightarrow (-M_x, M_y, M_z)$  and  $(P_x, P_y, P_z) \rightarrow (-P_x, P_y, P_z)$ . The reflection  $\sigma_h$  transforms  $(M_x, M_y, M_z) \rightarrow (-M_x, -M_y, M_z)$  and  $(P_x, P_y, P_z) \rightarrow (P_x, P_y, -P_z)$ , and so on. Using these transformations, we computed the invariants in each phase and listed them in the last few rows of Table I.

## Appendix C: Fermi lines in the staggered CSL

Let us briefly discuss how the anti-commutation relation  $\{\hat{\mathcal{H}}_{MF}, \sigma_v\} = 0$  in the staggered CSL leads to the emergence of line Fermi surfaces. Note that the  $\sigma_v$  changes the sign of stagger flux  $\phi$ . In staggered CSL, we can choose the hopping phase of all nearest neighbors as  $\arg(t_{ij}) = \pm\pi/2$  to satisfy  $\Phi_{\Delta/\nabla} = \pm\phi = \pm\pi/2$ . Then, changing the sign of the stagger flux  $\phi$  implies changing the sign of spinon hopping,  $\sigma_v : e^{\pm i\pi/2} = \pm i \rightarrow$

$e^{\mp i\pi/2} = \mp i$ . Therefore, the staggered CSL mean-field Hamiltonian satisfies  $\sigma_v \hat{\mathcal{H}}_{\text{MF}} \sigma_v = -\hat{\mathcal{H}}_{\text{MF}}$ , or equivalently  $\{\hat{\mathcal{H}}_{\text{MF}}, \sigma_v\} = 0$ . Then, for a  $\hat{\mathcal{H}}_{\text{MF}} = \sum_{\mathbf{k}, \sigma} \varepsilon(\mathbf{k}) \hat{f}_{\mathbf{k}\sigma}^\dagger \hat{f}_{\mathbf{k}\sigma}$ , the anti-commutation relation implies

$$\sigma_v \hat{\mathcal{H}}_{\text{MF}} \sigma_v = \sum_{\mathbf{k}, \sigma} \varepsilon(\sigma_v(\mathbf{k})) \hat{f}_{\mathbf{k}\sigma}^\dagger \hat{f}_{\mathbf{k}\sigma} = - \sum_{\mathbf{k}, \sigma} \varepsilon(\mathbf{k}) \hat{f}_{\mathbf{k}\sigma}^\dagger \hat{f}_{\mathbf{k}\sigma} \quad (\text{C1})$$

for every crystal momentum  $\mathbf{k}$ . Therefore, along the vertical mirror plane  $\sigma_v(\mathbf{k}) = \mathbf{k}$ ,  $\varepsilon(\sigma_v(\mathbf{k})) = \varepsilon(\mathbf{k}) = -\varepsilon(\mathbf{k}) = 0$ . Furthermore, since staggered CSL has  $C_3$  rotation symmetry, we eventually get three Fermi lines connected by  $C_3$  rotation and protected by anti-commutation relations.

#### Appendix D: Tricritical point

In the phase diagram shown in Fig. 1(b), we observe that the continuous transition between the Dirac chiral spin liquid (CSL) and the gapped CSL becomes discontinuous at the point marked by the black circle. This point, which separates the continuous transition from the discontinuous one along the phase boundary, is known as a tricritical point. In the following, we investigate the phase transition between the Dirac CSL and the gapped CSL by constructing the Landau-Ginzburg free energy through a symmetry analysis.

Based on symmetry considerations, the Landau-Ginzburg free energy involving the uniform chiral flux

$\theta$  and the staggered chiral flux  $\phi$  fields is expressed as

$$F_{\text{tot}} = F_\theta + F_\phi + F_{\theta\&\phi} \quad (\text{D1a})$$

$$F_\theta = u_1 \theta^6 + f(J_d, J_\chi) \theta^4 - h(J_d, J_\chi) \theta^2, \quad (\text{D1b})$$

$$F_\phi = \frac{1}{2} u_2 \phi^2 - \alpha J_\chi \phi, \quad (\text{D1c})$$

$$F_{\theta\&\phi} = g(J_d, J_\chi) \phi \theta^2. \quad (\text{D1d})$$

Here the coefficients  $f(J_d, J_\chi)$ ,  $g(J_d, J_\chi)$ , and  $h(J_d, J_\chi)$  are function of  $J_d$  and  $J_\chi$ , while  $u_1$ ,  $u_2$ , and  $\alpha$  are positive constants. By integrating out the  $\phi$  field, we study the effect of  $\phi$  fluctuations on the order of the phase transition through the effective free energy of  $\theta$ ,

$$F_\theta^{\text{eff}} = F_\theta - \frac{1}{2u_2} [\beta J_\chi - g\theta^2]^2 \equiv u_1(\theta^6 + p\theta^4 - q\theta^2).$$

The functions  $p$  and  $q$  are defined as  $u_1 p = f - g^2/2u_2$  and  $u_1 q = h - \beta J_\chi g/u_2$ . In the  $(p, q)$  parameter space, a second-order phase transition occurs when  $q$  goes from negative to positive with  $p > 0$ . Conversely, if  $p < 0$ , the system undergoes a first-order phase transition, with the boundary given by  $q = -p^2/4$ . Thus, the tricritical point appears at  $p = q = 0$ , indicating that the nature of the phase transition depends on the sign of  $p$ . This approach effectively describes the VMC phase diagram near the tricritical point.